JOURNAL OF SYNCHROTRON RADIATION

ISSN 1600-5775

Received 26 April 2019
Accepted 10 July 2019

Edited by I. Lindau, SLAC/Stanford University, USA

Keywords: storage ring; diffraction limit; laser slicing; undulator radiation; synchrotron light source; radiation background.

Laser-slicing at a low-emittance storage ring

Simone Di Mitri,[a]* William Barletta,[b] Anna Bianco,[a] Ivan Cudin,[a] Bruno Diviacco,[a] Lorenzo Raimondi,[a] Simone Spampinati,[a] Carlo Spezzani[a] and Claudio Masciovecchio[a]

[a]Elettra – Sincrotrone Trieste SCpA, Basovizza, 34149 Trieste, Italy, and [b]Department of Physics, Massachusetts Institute of Technology, Cambridge, MA, USA. *Correspondence e-mail: simone.dimitri@elettra.eu

Laser-slicing at a diffraction-limited storage ring light source in the soft X-ray region is investigated with theoretical and numerical modelling. It turns out that the slicing efficiency is favoured by the ultra-low beam emittance, and that slicing can be implemented without interference to the standard multi-bunch operation. Spatial and spectral separation of the sub-picosecond radiation pulse from a hundreds of picosecond-long background is achieved by virtue of 1:1 imaging of the radiation source. The spectral separation is enhanced when the radiator is a transverse gradient undulator. The proposed configuration applied to the Elettra 2.0 six-bend achromatic lattice envisages total slicing efficiency as high as 10^{-7}, one order of magnitude larger than the demonstrated state-of-the-art, at the expense of pulse durations as long as 0.4 ps FWHM and average laser power as high as ∼40 W.

1. Introduction

The last decade (∼2010 to date) has seen a renaissance of accelerator physics studies and technological advances in synchrotron light sources, aiming to improve the average spectral brightness and the transversally coherent fraction of photons by several orders of magnitude, in both the soft and hard X-ray wavelength ranges. A fourth-generation of low-emittance or diffraction-limited storage rings (DLSRs) has been announced (Borland, 2014). Such a breakthrough in spectral brightness and coherence comes, however, at cost of bunch durations typically longer than ∼15 ps r.m.s. (Martin, 2011). The natural bunch length is primarily set by the radiofrequency of the accelerating cavities, usually operating at 100 or 500 MHz. Additional bunch lengthening, on top of the aforementioned value and usually by a factor of two to four, is commonly induced by the electric field of a higher-harmonic cavity with the aim of suppressing either transverse or longitudinal beam instabilities, and increasing the beam Touschek lifetime. Bunch lengthening is mandatory in DLSRs also for minimizing the transverse emittance growth otherwise induced by intra-beam scattering in high charge density bunches (Leemann, 2014). Increasing the spectral brilliance and the fraction of coherent photons in the X-ray wavelength range at the expense of time resolution is therefore a general trend of low-emittance rings.

In the preceding decade (∼2000–2010), studies aimed in the opposite direction flourished: production of few tens of femtosecond long photon pulses in storage rings was proposed by Zholents & Zolotorev (1996), studied for implementation at several facilities (Zholents & Zolotorev, 1996; Ingold *et al.*, 2001; Nadji *et al.*, 2004; Yu *et al.*, 2011; Lau *et al.*, 2012; Prigent *et al.*, 2013), and eventually implemented at a few (Schoenlein

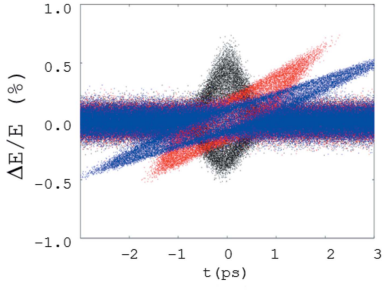

et al., 2000*a*,*b*; Khan *et al.*, 2006; Ingold *et al.*, 2001; Beaud *et al.*, 2007; Holldack *et al.*, 2014; Labat *et al.*, 2018). This approach targeted time-resolved experiments requiring low photon pulse energy and moderate average photon flux. For example, investigating reversible dynamics in molecular systems of different materials requires a non-destructive photon–matter interaction. Even in the case of samples surviving relatively high photon flux, space charge effects in photoelectron spectroscopy up to ablation may seriously compromise the collection of information about the sample properties. Storage rings therefore look like suitable light sources for experiments requiring a reduced peak photon flux, but accompanied by pulse repetition rates up to hundreds of MHz. Wide wavelength tunability can be provided, *e.g.* by dipole magnets and variable-gap insertion devices (IDs) in a series.

The next generation of X-ray free-electron lasers driven by superconducting linear accelerators will be able to offer similar performance at the expense of an attenuation of the radiation peak flux by many orders of magnitude, and up to 1 MHz repetition rate in continuous-wave mode. The wavelength tunability in free-electron lasers is typically limited to a few percent whereas, for example, extended X-ray absorption fine-structure and similar experimental techniques must access a far wider spectral range. For an exhaustive comparison of most advanced light sources, which is out of the aim of this article, we kindly send the reader to Schoenlein *et al.* (2019).

In spite of some successful implementations of femtoslicing at presently running third-generation synchrotron light sources, slicing has recently been given ever lower priority with respect to electron optics designs for diffraction-limited light sources. This trend is motived by the limited average photon flux per unit relative bandwidth typically achieved with femtoslicing, and by the conflict of the relatively large dispersion function required for spatial and/or angular filtering of the short radiation pulse with the typically small dispersion of diffraction-limited optics designs.

This work aims to demonstrate the possibility of improving the total slicing efficiency (and thereby the average spectral flux of the short radiation pulse) by one to two orders of magnitude with respect to existing solutions, at the expense of five to ten times longer (still sub-picosecond) laser pulses and about four times higher average laser power (in the range 30–60 W). This work also shows that the implementation of laser-slicing can be made transparent to the standard multi-bunch operation and optics design of a DLSR in the soft X-ray region. The low-emittance optics design of Elettra 2.0, the current design of which is based on a six-bend achromatic cell (Karantzoulis & Barletta, 2019; Karantzoulis, 2018), is considered as a case study. In Elettra 2.0, the dispersion function naturally excited in the arc cell is large enough to laterally separate by $\sim$0.5 mm the short radiation pulse from the hundreds of picosecond-long background. By imaging the radiation source with a 1:1 focusing system, the two light spots can be visualized downstream of the radiator; only one of the two is eventually selected for propagation to the sample, *e.g.* with a movable slit. The signal-to-noise ratio (SNR) at the sample is additionally enhanced by the relative spectral separation of the radiation emitted in a transverse gradient undulator (TGU). A total slicing efficiency of $\sim 10^{-7}$ [present state of the art is 10^{-8} (Holldack *et al.*, 2014) and typically approaching 10^{-9}] can be obtained with no impact on the lattice design; that is, the wiggler-modulator and the TGU-radiator can be installed without interference with the machine layout. In principle, the 12-fold, six-bend lattice of Elettra 2.0 is suitable for the simultaneous operation of additional (up to 12) beamlines in short radiation pulse mode.

The theoretical framework for the electron beam dynamics in the presence of laser-slicing in a storage ring was illustrated in the seminal work of Zholents & Zolotorev (1996). Here we elucidate the scaling laws of the laser-induced energy spread with laser sizes, electron beam sizes and wiggler length in a diffraction-limited storage ring (Subsection 2.1). We then discuss the different sources of radiation background from sliced and non-sliced electrons, either in the same bunch or in adjacent ones, and the main actions to be taken to minimize it. This discussion includes the proposal of a TGU-radiator and specifications for detector temporal gating (Subsections 2.2 and 2.3). Section 3 presents laser-slicing in Elettra 2.0. The electron beam dynamics and the effect of laser-slicing are followed along the ring and on successive turns. Three possible scenarios are envisaged as a function of the laser pulse duration and average laser power. Our findings are compared with results in the existing literature, both theoretical and experimental. We offer our conclusions in Section 4. We send the reader to Appendix *A* for explicit analytical expressions derived *ab initio* for the laser-induced energy modulation amplitude, the r.m.s. energy spread and the photon pulse duration. There, we put in evidence the approximations carried out by Zholents & Zolotorev (1996) and their range of validity, in comparison with expressions with exact numerical factors and including three-dimensional particle beam sizes and laser diffraction. The simulation studies presented in this article were first set on the basis of the expressions in Appendix *A*, and found in good agreement with the theoretical predictions.

2. Theoretical background

2.1. Scaling laws in low-emittance rings

In laser-slicing (Zholents & Zolotorev, 1996) an electron bunch interacts with an external, shorter laser pulse in a wiggler magnet installed in a dispersion-free section of a storage ring. Downstream, the laser-induced energy modulation translates into transversally spatial separation of the sliced electrons with respect to the beam core by virtue of a non-zero dispersion function. Here, electrons radiate in an undulator. Owing to the spatial and/or angular separation of sliced and non-sliced electrons, the short and the long radiation pulses can be separated and, depending on the photon transport layout, either the short or the long pulse reaches the detector.

In general, the higher the laser-induced energy modulation in the wiggler, the smaller the number of electrons pushed to

large energy offsets, $\Delta E/E$. However, a large energy offset is required to discriminate the short pulse duration from background (this is the radiation from the beam core of the sliced bunch, as well as radiation from other bunches). This observation suggests a compromise between radiation flux and SNR. The experimental results collected so far suggest a value for the ratio of the laser-induced energy modulation over the equilibrium energy spread $p = (\Delta E/E)_{\rm mod}/\sigma_{\delta,\rm eq} > 5$, and a ratio of the induced energy spread over the equilibrium energy spread larger than 3. These values typically translate into energy modulation amplitude in the range 0.5–1.0%. Since the on-axis energy modulation depends upon the transverse sizes of neither the laser spot nor the electron beam, the laser–electron interaction should be designed in a way that maximizes the laser-induced energy spread for any given energy modulation amplitude. For a deeper look, we consider equation (10) in Appendix *A* in the approximation $K \gg 1$. For any given laser pulse energy and laser wavelength, we find the following scaling law,

$$\frac{\Delta E_{\rm mod}}{E} \propto \frac{1}{\gamma}\left(\frac{N_{\rm u}}{N_{\rm L}}\right)^{1/2} \propto \frac{1}{\gamma}\left(\frac{L_{\rm u}}{\lambda_{\rm u} c\Delta t_{\rm L}}\right)^{1/2} \propto \frac{K}{\gamma^2}\left(\frac{L_{\rm u}}{c\Delta t_{\rm L}}\right)^{1/2}, \quad (1)$$

where we took advantage of the wiggler resonance condition. The relative energy spread shows, of course, the same dependence on K, electron beam energy and laser pulse duration. Its additional dependence on the electron beam and the laser beam transverse size can be discussed for two alternative scenarios, when either the laser spot is much larger than the electron beam or the laser is transversally matched to the electron beam envelope,

$$\frac{\sigma_{E,\rm mod}}{E} \propto \frac{K}{\gamma^2}\left(\int_0^{L_{\rm u}} \frac{{\rm d}s}{\sigma_{\rm L,w}\left(1+s^2/Z_{\rm R}^2\right)^{1/2}}\right)^2 \propto \left(\frac{L_{\rm u}}{\sigma_{\rm L,w}}\right)^2 \propto \frac{L_{\rm u}^2}{\lambda Z_{\rm R}} \propto \frac{L_{\rm u}}{\lambda}\bigg|_{L_{\rm u}\le Z_{\rm R}}, \qquad \text{for } \sigma_{\rm L} \gg \sigma_{\rm e}, \quad (2a)$$

$$\frac{\sigma_{E,\rm mod}}{E} \propto \frac{K}{\gamma^2}\left(\int_0^{L_{\rm u}} \frac{{\rm d}s}{\sigma_{\rm L,w}\left(1+s^2/Z_{\rm R}^2\right)^{1/2}}\right)^2 \propto \left(\frac{L_{\rm u}}{\sigma_{\rm L,w}}\right)^2 \propto \frac{L_{\rm u}^2}{\varepsilon_x \beta_{x,0}} \propto \frac{L_{\rm u}}{\varepsilon_x}\bigg|_{L_{\rm u}\le Z_{\rm R}\simeq\beta_{x,0}}, \qquad \text{for } \sigma_{\rm L} \simeq \sigma_{\rm e}. \quad (2b)$$

In the former case, equation (2*a*), a relatively long wiggler favours the accumulation of energy spread. Long wiggler periods (>10 cm) are allowed, which are compatible with relaxed K-values (<20), *i.e.* a weaker magnetic field (<2 T). The upper limit to the energy spread is given by the available longitudinal space for the wiggler, which can be several meters long (3–5 m). In the latter case, equation (2*b*), a squeezed laser size (<200 µm), corresponding to a very short Rayleigh length, forces the wiggler length to sub-meter length. This choice implies a short period (∼5 cm) and high K-values (>20), likely consistent with fields only available in superconducting or cryogenic devices (>2 T). Note that a higher electric field at the laser waist excited by a small laser transverse size does not necessarily imply a higher p-value: in fact, it would determine a larger energy spread if the wiggler were short enough to keep its length comparable with the Rayleigh length. Otherwise, the expected gain in energy spread is diminished by the reduced coupling efficiency along the wiggler. Making the wiggler longer would not help much because the laser is diffracting rapidly, thus weakly coupling to the electrons far from the waist location.

Both expressions in equation (2) show that, by virtue of smaller electron beam sizes and for the same wiggler and laser parameters, a low-emittance storage ring tends to increase the laser-induced energy spread with respect to third-generation light sources. In particular, the laser electric field can be locally enhanced by a smaller laser spot along the wiggler. A laser size as small as 500 µm r.m.s. (∼0.25 mm × 0.25 mm compared with ∼1 mm × 1 mm laser transverse section at present femtoslicing facilities) still generates an electric field that is sampled uniformly by the electrons. In this way a double-horn energy distribution of the sliced electrons can be generated, as shown in the next section. Such a distribution determines, in turn, a larger fraction of sliced electrons at the maximum off-energy level with respect to that induced by a laser size perfectly matched to the electron beam size. Finally, a lower emittance favours the spatial/angular separation of the short pulse radiation from the whole bunch emission, *i.e.* a higher SNR.

2.2. Spatial, angular and spectral separation of emitted radiation

The spatial and angular separation of the radiation emitted by the sliced electrons entering a dipole magnet or an undulator is determined by the value of the energy dispersion function and its longitudinal derivative at the radiator,

$$\Delta x > \eta_x \delta_{\rm min}, \qquad \Delta x' > \eta_x' \delta_{\rm min}, \quad (3)$$

where $\delta_{\rm min}$ is intended to be the minimum relative energy offset within the energy distribution of laser-sliced electrons.

The separation of radiation emitted by the laser-sliced electrons from that emitted by all other electrons can be increased by the spectral difference of photons emitted, *e.g.* in a TGU, the field gradient being in the horizontal plane. A monochromator installed downstream of the TGU would then contribute to select the short radiation pulse, in addition to the spatial/angular separation described above. This separation increases the SNR with respect to the pure spatial/angular collimation of the radiation. A TGU is characterized by a magnetic field gradient $\alpha_{\rm TGU} = (\Delta K/K)(1/\Delta x)$. We recall that, for $K \gg 1$, the undulator resonance condition leads to $(1/N_{\rm u}) = \Delta\lambda/\lambda \cong 2\Delta K/K$. To have a net spectral separation, we require that the difference in photon wavelength with respect to the central undulator wavelength due to the lateral displacement of the particles be larger than the natural bandwidth of undulator radiation evaluated as if it were a standard undulator: $\Delta\lambda_{\rm TGU}/\lambda \cong 2\Delta K_{\rm TGU}/K \gg \Delta\lambda/\lambda$, or, equivalently,

Table 1
Radiation background and mitigation strategies.

	Source of background radiation	Pulse duration, FWHM (ps)	How to suppress it
a	Non-sliced electrons in the laser-sliced bunch, at small betatron amplitudes	∼100	Spatial, angular, spectral separation (photon mask, monochromator)
b	Non-sliced electrons in the laser-sliced bunch, at large betatron amplitudes	∼100	Monochromator; low-emittance optics
c	Non-sliced electrons in stored bunches, at small betatron amplitudes	∼100	Spatial, angular, spectral separation (photon mask, monochromator)
d	Non-sliced electrons in stored bunches, at large betatron amplitudes	∼100	Monochromator; low-emittance optics; detector temporal gating
e	Sliced electrons in the same laser-sliced bunch, after first turn emission	∼1	Multi-bunch slicing operation; detector temporal gating
f	Sliced electrons in other laser-sliced bunches, after first turn emission	∼1	Multi-bunch slicing operation; detector temporal gating

$$\alpha_{\rm TGU}\Delta x \simeq \alpha_{\rm TGU}\,\eta_x\,\delta_{\rm mod} = \frac{\Delta K_{\rm TGU}}{K} \gg \frac{1}{2N_{\rm u}}. \quad (4)$$

Inserting the definition of the p-parameter, equation (4) becomes

$$2pN_{\rm u}\alpha_{\rm TGU}\,\eta_x\,\sigma_{\delta,{\rm eq}} \gg 1. \quad (5)$$

The adoption of a TGU in a dispersive region introduces two perturbations to the beam dynamics. First, the electron optics and the closed orbit are distorted. Second, the damping partition numbers, *i.e.* the damping times, and the beam equilibrium emittances are modified. These considerations have been taken into consideration in the following study for Elettra 2.0.

2.3. Background radiation

Different types of radiation background and techniques to minimize it are described in Table 1. The background of type *a* and *c* ('core' background) is suppressed primarily by spatial and/or angular separation of the radiation. The same separation method applies to radiation background of type *b* from electrons at large betatron amplitudes ('tail' background). This method typically requires an angular separation of ∼1 mrad at the source, corresponding to several millimeters at the front-end of the beamline, where a slit can be applied to mask the unwanted radiation. Background of type *b* is also minimized by a small natural emittance (for any given betatron amplitude, fewer electrons reach large lateral and angular offsets from the core) and by spectral filtering of the emitted radiation with a monochromator (laser-sliced, off-energy electrons emit at a slightly different central wavelength than on-energy electrons). Identical considerations apply to the background of type *d*.

The background of type *e* ('halo' background) is due to radiation emitted by those electrons that, after interacting with the laser, maintain their off-energy amplitude of transverse oscillation over a time scale shorter than the transverse damping time, τ_x. In one turn, those electrons shift longitudinally by ∼1 ps or so by virtue of the storage ring momentum compaction and of their energy offset. Hence, the radiation emitted at turns successive to the interaction with the laser should not be collected. It has been demonstrated (Streun, 2003; Schick *et al.*, 2016) that alternating interactions with M bunches in the ring (slicing in 'sequence mode') allows one to increase the repetition rate of sliced pulses up to the level of ∼100 Hz × M, provided that fast shutters or gating of the detector with rise and fall time shorter than ∼432/M ns (864 ns is the revolution period in Elettra 2.0) are available to block halo radiation from the other bunches. State-of-the-art synchronization of femtosecond laser amplifier with the storage ring allows the slicing process to alter between three bunches on the multi-bunch train with a mutual temporal delay of 12 ns (Holldack *et al.*, 2014). We propose to push this scheme to four or ten bunches devoted to slicing, and therefore we will require gating rise and fall time of the order of 40–100 ns.

As explained by Streun (2003), chromatic filamentation, due to the unavoidable nonlinear optics elements in the ring lattice, contributes to generate a uniform halo of particles around the beam core at time scales shorter than τ_x. On the one hand, the formation of a halo is expected to generate background of constant intensity. On the other hand, filamentation randomizes the electrons' position and angle at the source point such that, in a realistic scenario of finite spatial and angular acceptance of the beamline, the background signal intensity collected at the detector tends to oscillate, while being exponentially suppressed overall on a time scale intermediate to the revolution period (∼1 µs) and the damping time (∼10 ms) (Holldack *et al.*, 2014; Schick *et al.*, 2016). We estimate the condition for full filamentation by the relative betatron phase advance and the particle relative energy offset, $\Delta\mu_x\delta \geq 1$. If $T_{\rm riv}$ is the revolution period, $T_{\rm fil}$ is the time needed to achieve full filamentation, and $Q_x = \Delta\mu_x/2\pi$ is the betatron tune, we can re-write that condition

$$2\pi Q_x\sigma_{\delta,{\rm mod}}\,\frac{T_{\rm fil}}{T_{\rm riv}} \geq 1. \quad (6)$$

For parameters typical in a <3 GeV low-emittance ring such as $Q_x \simeq 30$, $\sigma_{\delta,{\rm mod}} \simeq 0.4\%$ and $T_{\rm riv} \simeq 1$ µs, we estimate $T_{\rm fil} \geq 1$ µs. We expect an overall transverse damping of the background signal on a time scale intermediate to $T_{\rm fil}$ and τ_x, *e.g.* a fraction of a millisecond or so. This order of magnitude matches the observations reported by Holldack *et al.* (2014) and Schick *et al.* (2016). In conclusion, the repetition rate of short radiation pulses generated by the same bunch and detected at one beamline with much reduced background signal is expected to be in the frequency range 1–10 kHz. This single pulse repetition rate is then multiplied by the number of sliced bunches in the stored train. The effective total repetition rate will define the laser frequency, if not additionally constrained by the maximum practical average power of the laser.

3. Laser-slicing at Elettra 2.0

3.1. Single-bunch dynamics

In this section we analyse the dynamics of a single electron bunch through the wiggler (modulator) and a downstream undulator (radiator) in the Elettra 2.0 lattice. We assume radiation emitted in the keV-photon energy range. We then follow the beam dynamics by particle tracking for three consecutive turns. The wiggler is assumed to be installed in one of the 4.62 m-long dispersion-free straight sections of Elettra 2.0. The radiator is installed in a 1.68 m-long dispersive region inside the cell. This arrangement does not require any modification to the low-emittance optics of Elettra 2.0. Moreover, the ∼3 m-long modulator can share the straight section with an additional ∼1 m short undulator, *e.g.* in canted configuration. The radiator is installed in a short dispersive straight section typically not used by ID-based photon beamlines. No additional dipole magnets or correctors are required for radiation separation, as we will see in the following.

A list of parameters of Elettra 2.0 and of the associated laser-slicing setup is given in Table 2. At this stage of the study, the filling pattern is assumed to be uniform, *i.e.* all bunches have the same 0.8 nC charge and their separation is 2 ns (the RF frequency is 500 MHz). The bunch length at equilibrium, as reported in Table 2, is computed with the lengthening effect of a third-harmonic cavity already in place. Radiation background is not considered in this section, which primarily aims to validate the analytical laser-induced energy modulation (see Appendix *A*) with particle tracking. Additional considerations about background and hybrid filling pattern will be discussed in Section 4.

The *elegant* code (Borland, 2000) was used to track a single electron bunch from the entrance of the wiggler to the same point after three turns. Fig. 1 shows the electron beamline from the dispersion-free straight section, where the wiggler is installed, to the end of the six-bend arc cell. The radiator is installed in the middle of the arc, where the dispersion function (blue line) is maximal. The transverse r.m.s. beam size at equilibrium in the wiggler and in the radiator is approximately 60 µm in the horizontal plane and 7 µm in the vertical (1% betatron coupling is assumed).

The effect of the interaction with a 0.8 ps FWHM-long, 3 mJ-energy Gaussian and Fourier transform limited laser pulse is illustrated in Fig. 2. The peak energy deviation and the r.m.s. energy spread induced by the laser interaction are, respectively, nine and three times larger than the natural energy spread, in agreement with the analytical prediction. Since the laser spot size that maximizes the interaction with the electrons is approximately 550 µm (as predicted by tracking studies and in rough accordance with the theoretical prediction, see Appendix *A*), and hence much larger than the electron size, the electrons are collected into a double-horn energy distribution (see inset in the top plot). This distribution is expected to facilitate suppression of background radiation from non-sliced electrons (see Section 3 later). On a single-pass basis, the interaction increases the projected value of the r.m.s. relative energy spread from 0.07% to 0.08%. After three turns, the sliced electrons are longitudinally shifted from the interaction region due to the momentum compaction of the storage ring. Fig. 3 shows how the longitudinal phase space evolves immediately after the laser interaction and for the successive two turns. Depletion of electrons from the region of laser interaction induces current ripples at its edges.

Table 2
Parameters of Elettra 2.0 and laser-slicing; a uniform filling pattern is assumed.

	Value	Units
Storage ring		
Beam mean energy	2.0	GeV
Circumference length	260	m
Achromatic cell type	Six-bend	
Revolution period	0.867	µs
RF bucket spacing	2	ns
Harmonic number	433	
Filling pattern	93	%
Average current, total	400	mA
Longitudinal damping time	15	ms
Bunch charge	0.8	nC
Single-bunch average current	1	mA
Bunch duration, FWHM	54	ps
Relative energy spread, RMS	0.070	%
Transverse geometric emittance, RMS (x, y)	0.4, 0.004	nm rad
Linear momentum compaction	2×10^{-4}	
R_{51}, R_{52} from wiggler to radiator	$<10^{-5}$	rad, m
R_{56} from wiggler to radiator	2.2	mm
Total length of straight section (wiggler)	4.5	m
Total length of dispersive section (radiator)	1.6	m
Wiggler		
Number of periods	30	
Period length	120	mm
Total length	3.6	m
Wiggler parameter, K	22.6	
Peak magnetic field	2.0	T
Horizontal betatron function at waist	9	m
Vertical betatron function at waist	3	m
Horizontal electron beam size at waist, RMS	60	µm
Vertical electron beam size at waist, RMS	3	µm
Laser–electrons interaction		
Wavelength	1.0	µm
Duration, FWHM	0.8	ps
N_u/N_L	0.125	
Size at waist, RMS	550	µm
Pulse energy	3	mJ
$\sigma_{\delta,eq}/\sigma_{\delta,0}$	<1.5	
On-axis energy modulated amplitude, predicted / simulated	13 / 12	MeV
p-parameter	6.3	
Induced relative energy spread r.m.s., predicted / simulated	0.40 / 0.36	%
$\sigma_{\delta,mod}/\sigma_{\delta,0}$	5	
Electron capture efficiency	0.13	
Electron slice duration at radiator, FWHM	0.8	ps
Radiator – undulator		
Number of periods	25	
Period length	40	mm
Total length	1.0	m
Undulator parameter, K	2	
Harmonic number	3	
Photon energy	950	eV
Horizontal average betatron function	3.5	m
Horizontal average dispersion function	0.06	m

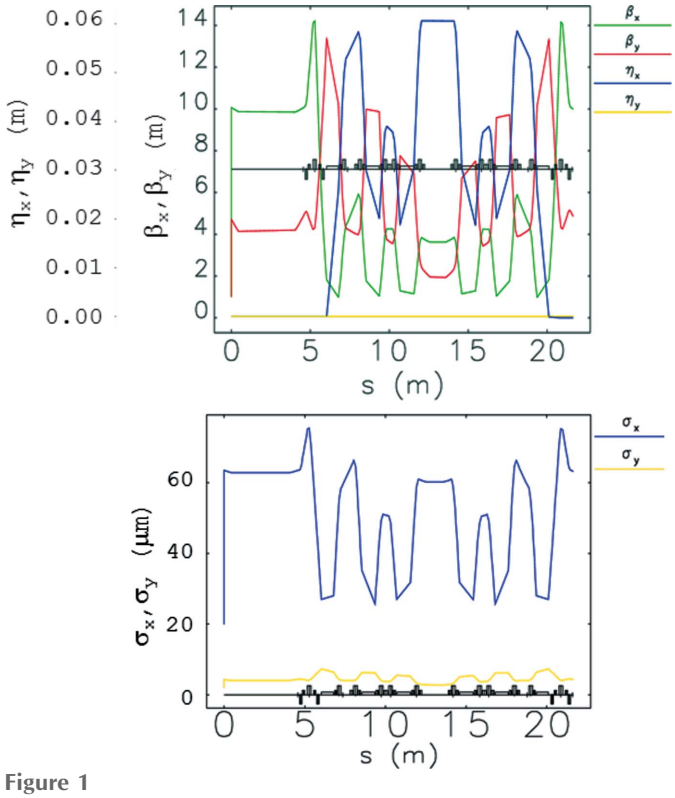

Figure 1
Top: linear optics functions from the beginning of the dispersion-free straight section, which accommodates the wiggler, to the end of the six-bend arc cell. The radiator is installed in the dispersive section in the middle of the arc. Bottom: r.m.s. electron beam sizes at equilibrium through the beamline.

3.2. Coherent THz emission

The depletion of electrons one turn after the laser interaction generates a current ripple that emits coherent THz radiation. The depletion persists for a few thousand of turns, and its detection can be used to synchronize the laser pulse with the electron bunch, as predicted by Schoenlein *et al.* (2000*a*,*b*), experimentally observed by Holldack *et al.* (2006) and Byrd *et al.* (2006), and successfully applied at other facilities (Labat *et al.*, 2018). Fig. 4 shows the bunch current profile (normalized to the peak value) simulated after a single laser interaction at successive points of maximum dispersion, in the middle of the arcs, and downstream of the wiggler. The plots show that the formation of a 1 ps-long hole in the current profile is completed in one turn; *i.e.* the contrast of charge density becomes maximum and the current spikes become symmetric around the interaction region, one turn after the laser–electron interaction. Fig. 5 shows, at the top, the corresponding normalized current profile in the region of laser interaction, immediately after laser-slicing, and for the successive two turns. The lower plot shows the Fourier transform of the longitudinal charge distribution (bunching factor) at each turn. Enhanced radiation in the frequency range 0.5–3 T Hz is expected.

In spite of the low momentum compaction of Elettra 2.0 (see Table 2) – momentum compaction in DLSRs is at least one order of magnitude lower than in third-generation light

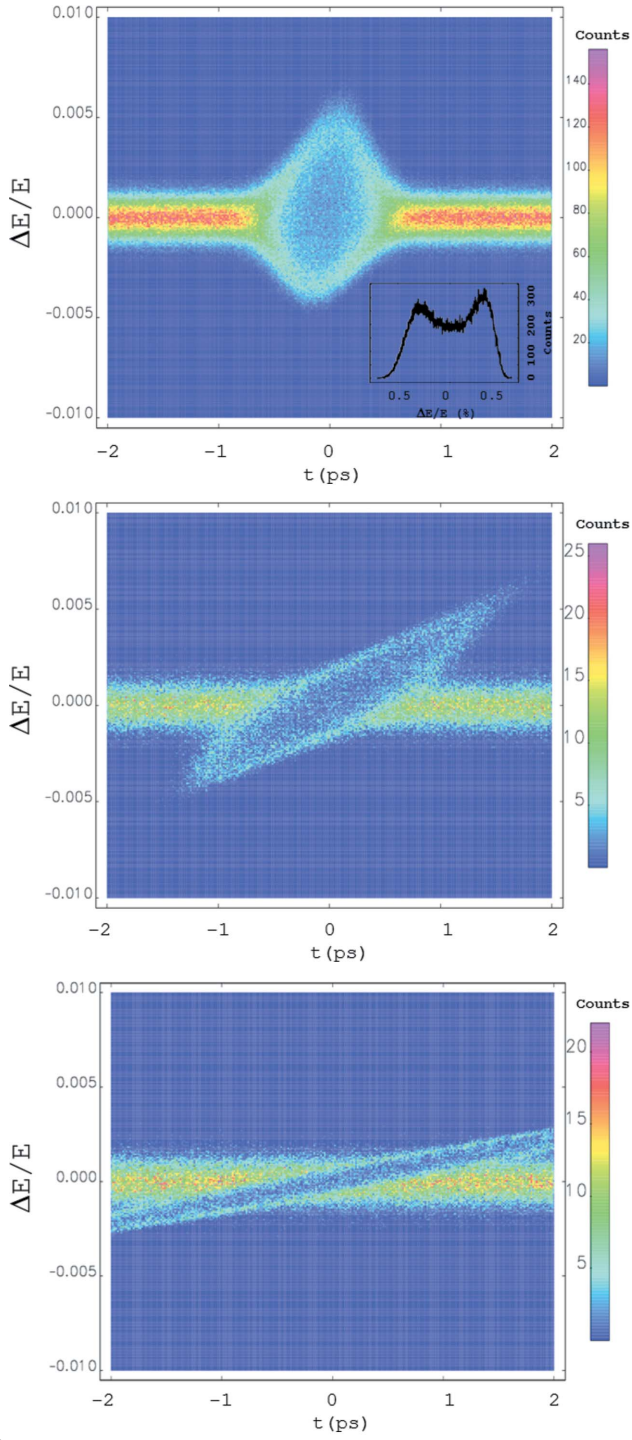

Figure 2
Contour plot of longitudinal phase space of the electron bunch at the radiator, immediately after laser-slicing (top), after one turn (middle) and after three turns (bottom).

sources – the reduction of the single-bunch peak current threshold for the burst emission of coherent synchrotron radiation (microwave instability) (Venturini & Warnock, 2002; Bane *et al.*, 2010) is alleviated by the relatively long bunch duration ensured by the high harmonic cavity. The 1D CSR (coherent synchrotron radiation) instability threshold in Elettra 2.0 at 2.0 GeV turns out to be ∼7 mA for the single

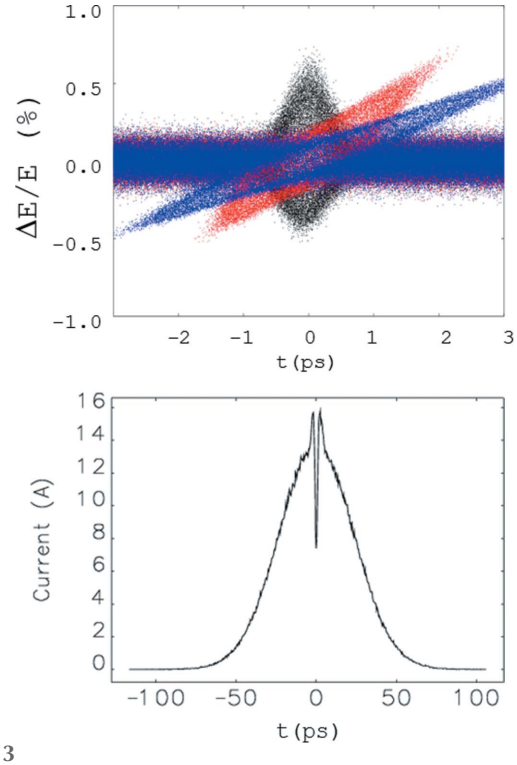

Figure 3
Top: longitudinal phase space after one laser interaction. Black: pass 0; red: pass 1; blue: pass 2. The peak energy deviation induced by the 3 mJ laser pulse is nine times larger than the natural energy spread. Bottom: bunch current profile after three turns. Depletion of electrons from the region of laser interaction induces current ripples at its edges.

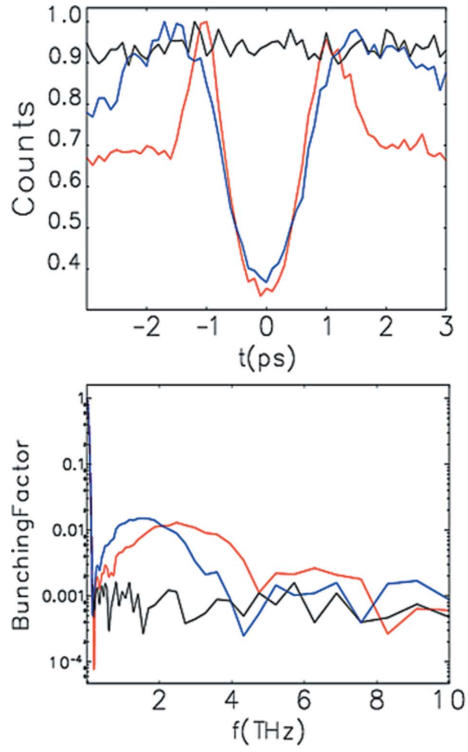

Figure 5
Normalized current profile at the radiator (top) and corresponding bunching factor (bottom), after one laser interaction. Black: pass 0; red: pass 1; blue: pass 2. Full depletion of electrons over a 1 ps FWHM-long region happens after one turn from the interaction, and persists for a few thousands of turns (only three turns shown).

bunch average current, where no 2D suppression of CSR emission by the vacuum chamber is taken into account. This estimate provides a safe margin for stable slicing operation with increased charge in sliced bunches.

3.3. Electron beam: spatial and energy distribution

The upper plot of Fig. 6 shows that for the electron beam and laser parameters of Table 2 the sliced electrons suitable for spatial and spectral separation of the emitted radiation are sitting at positive lateral coordinates, between 200 and 500 μm, with respect to the longitudinal axis of the beam, at the location of the radiator. The lower plot of Fig. 6 quantifies the percentage of off-energy particles with respect to the amount of particles on-energy. The total percentage of particles with a positive p-factor larger than five, *i.e.* energy modulation amplitude exceeding 0.4%, is approximately 0.5%. Fig. 7 illustrates the transverse phase space of the beam at the radiator for the first three consecutive turns after interaction with the laser. According to these results, we anticipate that a slit selecting lateral coordinates $x > 250$ μm in the proximity of the source point or, in a practical scenario, of its 1:1 image downstream of the radiator, would suffice for selecting sliced electrons with $p > 5$. A single-turn gated detector could then be used to eliminate radiation pulses longer than 1 ps, which are emitted by sliced electrons on successive turns.

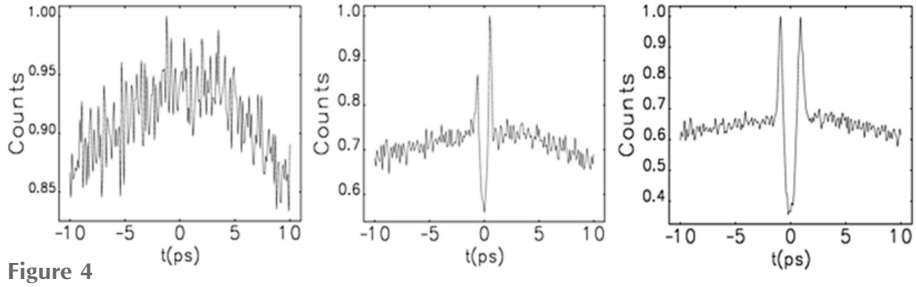

Figure 4
Current profile normalized to the peak value, zoomed in the proximity of the region of laser interaction. From left to right: in the middle of the dispersive section immediately following the wiggler (see also Fig. 1), in the analogous section after three achromats, in the analogous section after six achromats. All plots refer to the first turn after slicing.

Most of the short-pulse radiation is emitted by electrons with a relative energy deviation $\Delta E/E \geq 0.5\%$. For an undulator field gradient of 100 T m^{-1} and a dispersion function of 0.06 m at the radiator, the relative variation of undulator parameter from the on-axis value sampled by the off-energy electrons would be 3%, *i.e.* the relative photon energy difference would be approximately 6%. For comparison, the same 25-period undulator with no field gradient would provide a full-width spectral bandwidth of the order of

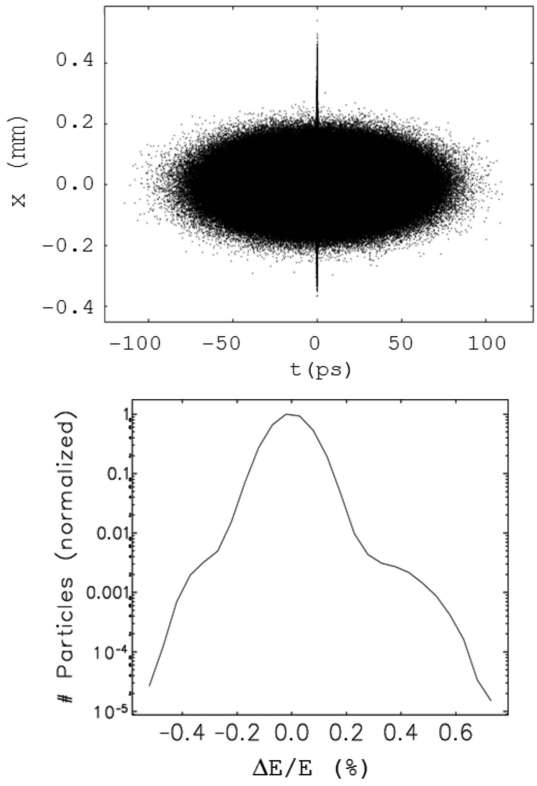

Figure 6
Top: the transverse position of electrons at the exit of the radiator *versus* longitudinal coordinate internal to the bunch. The energy-modulated electrons separate from the beam core at a positive lateral distance >250 μm from the reference trajectory. At the radiator location there is no angular separation because the derivative of the energy dispersion function is zero (see Fig. 1, lower plot). Bottom: number of electrons *versus* relative energy deviation, normalized to the number of particles on-energy. The fraction of particles with a positive *p*-factor > 5 is approximately 0.5%.

$1/N_u = 4\%$. In that case, the separation in photon energy of the short pulse from background would only be due to the energy difference of the modulated electrons, *i.e.* 1%, and therefore within the natural bandwidth of the undulator.

3.4. Undulator radiation: spatial and spectral distribution

Radiation emission from a linearly polarized planar undulator was simulated with the *SPECTRA* code (Tanaka & Kitamura, 2001). This preliminary study aims to illustrate the scheme of suppression of the long radiation pulse (background) by virtue of the pure spatial separation of the short and long pulse, and removal of the long pulse by a slit. This provides a first estimate of the ratio of the two pulse intensities at the 1:1 focusing plane.

The undulator parameters are listed in Table 2; the electron beam and the laser parameters are those of Option 3 of Table 3 (see below). This takes into account a hybrid filling pattern of the stored bunched, *i.e.* higher bunch charge for bunches involved in the slicing. By virtue of a higher laser peak power – we now consider a 0.4 ps FWHM-long laser pulse instead of the 0.8 ps-long pulse in Table 2 – the relative energy modulation amplitude becomes 0.9% and the horizontal distribution of sliced electrons at the radiator location extends up to

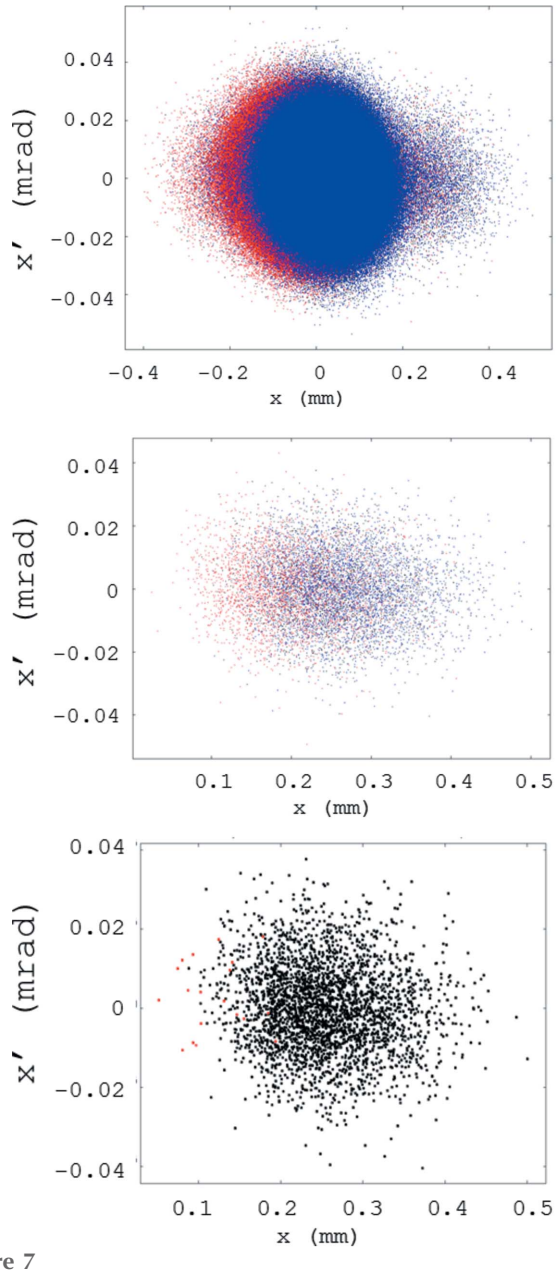

Figure 7
Transverse phase space at the radiator, immediately after laser interaction (black dots), after two turns (blue dots), after three turns (red dots). From top to bottom: whole beam, only particles at $\Delta E/E >$ 0.4% (*p*-factor > 5), only particles at $\Delta E/E > 0.4\%$ and within 1 ps time window centred on the laser interaction region.

660 μm off the beam axis. Approximately 0.5% of the total bunch charge is the fraction of particles with energy deviation $\Delta E/E > 0.8\%$, and can be found at horizontal coordinates larger than 400 μm at the radiator.

The third-harmonic spectral flux density spatial distribution (949 eV photon energy) was calculated at the virtual source point. Such a spatial distribution can be replicated downstream with a 1:1 optical focusing system, with a horizontal slit placed at the focal plane. In Fig. 8, the blue peak is the radiation pattern of the entire bunch train, averaged over one orbit; it is centred at $x = -480$ μm. A horizontal slit absorbs the radiation at horizontal coordinates $x < -180$ μm (or

Table 3
Parameters of Elettra 2.0 for laser-slicing with hybrid filling pattern.

	Option 1	Option 2	Option 3	Units
Storage ring				
Number of bunches devoted to slicing	10	4	4	
Time separation from train	±6	±10	±10	ns
Filling pattern	86	93	93	%
Average current, total	344	376	376	mA
Bunch charge	0.8	4.8	4.8	nC
Single-bunch average current	1	6	6	mA
Horizontal geometric emittance	0.4	0.8	0.8	nm rad
Wiggler				
Horizontal Electron beam size at waist, RMS	60	85	85	μm
Vertical electron beam size at waist, RMS	5	7	7	μm
Laser–electrons interaction				
Duration, FWHM	0.8	0.4	0.4	ps
Size at waist, RMS	550	600	600	μm
Pulse energy	3	4	3	mJ
Pulse frequency	10	10	20	kHz
Average power	30	40	60	W
On-axis energy modulation amplitude	13.3	21.7	18.8	MeV
p-parameter	6.3	9.1	7.8	
Electron slicing efficiency (η_1)	0.13	0.11	0.12	
Induced relative energy spread, RMS	0.36	0.59	0.51	%
$\sigma_{\delta,\mathrm{mod}}/\sigma_{\delta,0}$	5.1	7.4	6.4	
Slicing total efficiency	0.5×10^{-7}	1.1×10^{-7}	2.4×10^{-7}	
Radiator – undulator				
Spectral intensity in central cone	0.4×10^{8}	1.0×10^{8}	2.1×10^{8}	photons s^{-1} (0.1% bandwidth)$^{-1}$
Radiator – dipole magnet				
Spectral angular intensity	0.5×10^{6}	1.3×10^{6}	1.4×10^{6}	photons s^{-1} mrad^{-1} (0.1% bandwidth)$^{-1}$
Detector gating				
Halo radiation decay time	100	70	80	μs
Frequency of sampling	10	10	20	kHz
Time for detector switching	6	10	10	ns

300 μm from the undulator central axis). In red is the emission from a single sliced bunch, whose centre was chosen as the origin of the x-axis (see inset). The spatial distribution of the sliced electron bunch is assumed to be Gaussian with a standard deviation σ_x = 70 μm and dominated by the chromatic particles motion (the actual sliced electron distribution would be an asymmetric Gaussian still peaked where the short radiation pulse is in Fig. 8; such an asymmetry, however, is not that pronounced, as shown in Fig. 7). The ratio of the spatial spectral flux density emitted by the sliced (single bunch) and non-sliced electrons (train of bunches) over one orbit and calculated on the emission axis of the short pulse ($x = y = 0$) is at least as large as 1000.

In order to identify major distortions possibly induced by slope errors of the first mirror of the 1:1 focusing system, the radiation spatial distribution at the focal plane (where the slit is supposed to be installed) was simulated with the *Shadow* code (Cerrina & Rio, 2009). Radiation sources are still modelled as Gaussian distributions, which allows us to point out distortions or asymmetries of the radiation spot due to the mirror slope error. A cylindrical mirror working at 1° grazing incidence angle (α) and providing a 1:1 horizontal sagittal focusing (with 0.1 μrad tangential and 1 μrad sagittal r.m.s. slope error) is placed 7.5 m downstream of the radiator. Fig. 9

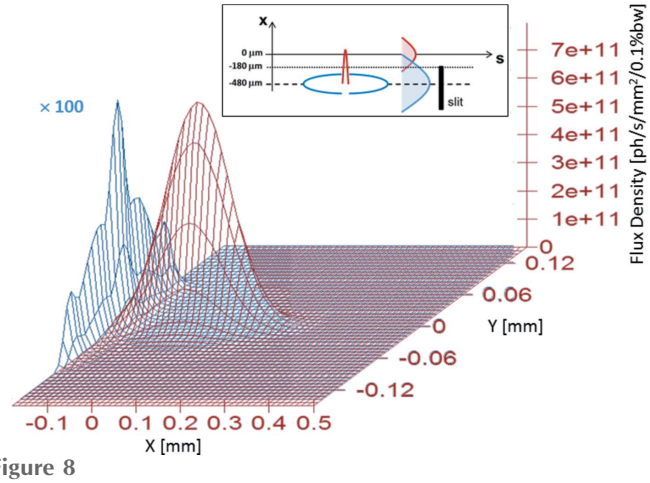

Figure 8
Inset: schematic of spatial filtering of radiation emitted by non-sliced electrons at the radiator image plane. The $3\sigma_x$ beam size of the non-sliced electron beam is approximately 200 μm at the source point (see electron distribution in Fig. 7). Tail radiation from particles at large betatron amplitudes extends up to ∼500 μm from the beam central axis (x = −480 μm in the inset). A slit absorbs the radiation up to 300 μm (x = −180 μm) from the undulator axis. In the main plot: spectral flux density from sliced (red curve) and non-sliced electrons (blue curve), after removal of tail background radiation by the slit. The blue curve is multiplied by a factor 100 for better visibility. Around x = 0, where the short photon pulse radiation is centred, the short pulse intensity is at least 10^3 larger than the residual background radiation.

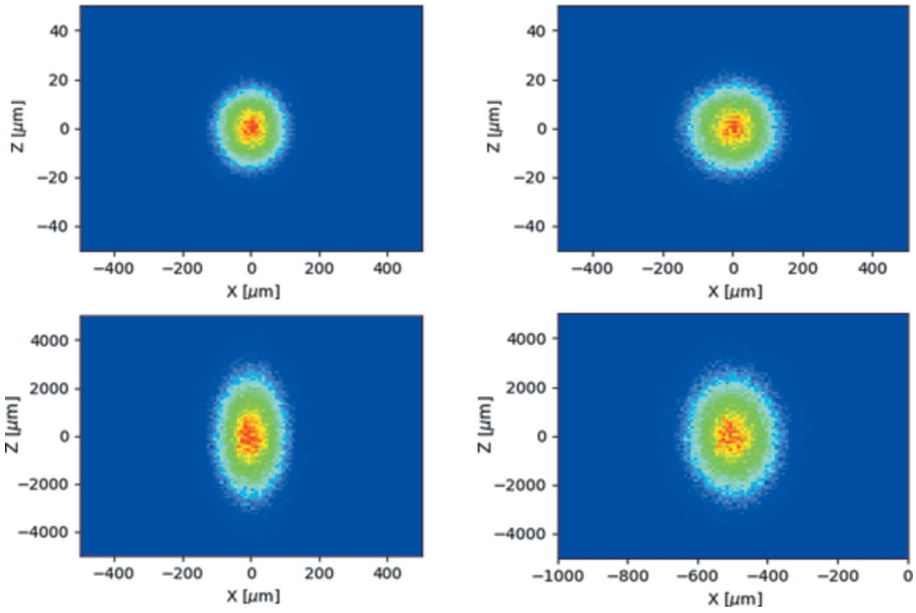

Figure 9
Simulations of spatial normalized intensity distribution of the long (left) and short (right) photon pulse at the source point (top), and at the horizontal focal plane 15 m downstream (bottom). The grazing incidence angle is 1°, the curvature radius is 13 cm, the reflectivity of the selected Rh coating is 80%. The short pulse is emitted 480 μm from the long pulse, in the horizontal plane. The sagittal focusing mirror is placed 7.5 m downstream of the source, and has a sagittal slope error of 1 μrad r.m.s. Colour code is normalized to peak intensity: on a single pulse basis, the short pulse (right) is about three orders of magnitude less intense than the long one.

shows the simulated distributions on the focal plane, 15 m from the radiator. The choice of sagittal focusing has been dictated by the ratio of tangential and sagittal scattering, which is lower in the second case by a factor of about $1/\tan\alpha$ (Raimondi & Spiga, 2015). Heat-load calculations reveal that a water-cooling system with standard parameters at Elettra is sufficient for the mirror, and therefore no image quality degradation due to thermal effects is expected. This simulation does not highlight any serious concern for the slope error of 1 μrad r.m.s., and confirms the feasibility of the focusing scheme.

In addition, the scattering contribution originating from the micro-roughness of the mirror surface was evaluated with *WISEr* (Raimondi *et al.*, 2013; Raimondi & Spiga, 2015). This allows us to quantify the contamination of the long pulse average photon flux tail onto the short pulse peak. The computation was performed in the worst-case scenario of longitudinal scattering, assuming a micro-roughness r.m.s. amplitude of 0.5 Å. Considering that sagittal scattering is lower by about a factor of 57 as compared with longitudinal scattering, we estimate that the ratio between the long pulse peak intensity and its sagittal scattering contribution ∼500 μm away from the optical axis is about 1.6×10^{10} (see Fig. 10). With a slicing efficiency of 10^{-7} (see Table 3 below), the predicted signal-to-noise ratio (short pulse intensity over background) at such a position is therefore ∼1000 in a realistic situation and with a high-quality mirror surface.

Spectral filtering of the background radiation can be added to the spatial filtering. In Fig. 11, the flux density (normalized to peak value) observed along a direction at $x = 480$ μm from the radiator axis is calculated with *SPECTRA* for, respectively, on-energy non-sliced electrons (black), off-energy sliced

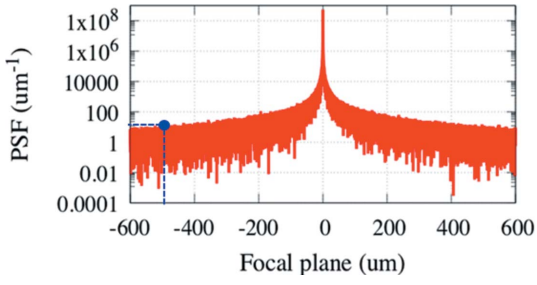

Figure 10
Point spread function (PSF) of the long pulse at the focal plane, as simulated by *WISEr* in the longitudinal scattering configuration. The SNR between the peak and the value at 480 μm from the optical axis (blue dot, where the short radiation pulse is centred) is about 2.8×10^8. Sagittal scattering is lower by about a factor of 57 as compared with longitudinal scattering, so that the ratio between the long pulse peak intensity and its sagittal scattering contribution 480 μm away from the optical axis, where the short pulse is located, is about 1.6×10^{10}.

electrons (red), and for the sliced electrons passing through a TGU with relative field gradient $\alpha = 100$ m^{-1} (green). A pure horizontal field gradient is simulated in *SPECTRA*: though this model does not simulate in a consistent manner the focusing effect of the TGU on the electrons motion, it is able to correctly predict the spectral properties of the emitted radiation. The impact of the TGU focusing properties on the beam dynamics was treated with the *elegant* code, as reported below.

The central photon energy difference of radiation emitted by sliced and non-sliced electrons is increased from 1.5% for a standard undulator with uniform field to 9% for a TGU. Owing to the field gradient, the bandwidth of the signal emitted by the sliced electrons is expected to be larger than

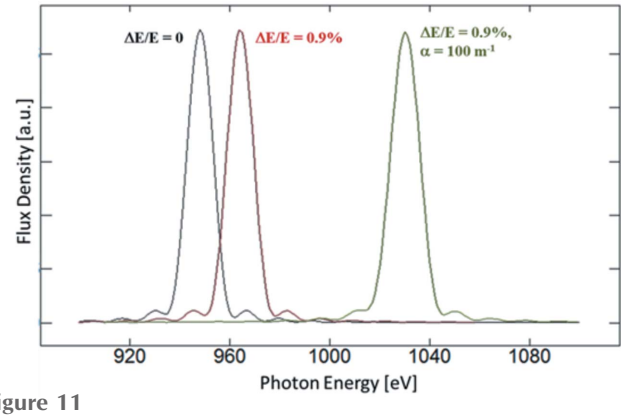

Figure 11
Normalized spectral flux density calculated at the third harmonic, at x = 480 µm from the radiator axis, emitted by on-energy electrons (non-sliced; black curve), off-energy electrons (sliced; red curve), and by off-energy electrons in the presence of a 100 m^{-1} undulator magnetic field gradient. The adoption of a TGU as a radiator fully de-couples the spectral component of radiation emitted by sliced and non-sliced electrons.

the bandwidth from a planar undulator. Nevertheless, since the horizontal size of the sliced electrons participating to most of the short pulse emission is of the order of 50 µm only, the actual bandwidth enlargement due to the field gradient is small (<10%) – and barely visible in Fig. 11 – compared with the natural bandwidth of a pure planar undulator emission.

The impact of a TGU with α = 100 m^{-1} installed in a dispersive region (η_x = 0.06 m) on the beam closed orbit, linear optics and partition numbers of Elettra 2.0 were evaluated through particle tracking. The orbit deflection is easily recovered by steering magnets installed all across the TGU section. The linear optics asymmetry is partially compensated by tweaking quadrupole magnets' strengths; the residual linear optics asymmetry (beta-beating) induced by the TGU is ∼1%. The horizontal emittance grows by ∼5%. This effect, however, is comparable with that of a realistic full set of beamline undulators and machine errors. Still, these preliminary considerations indicate that the installation of several TGUs in analogous dispersive regions for, for example, supplying multiple short pulse beamlines, would start affecting the brilliance at a non-negligible level. In this case, and depending upon users requirements, dedicated ultra-low-emittance runs could be conceived as an alternative operation to slicing; this would still be operated in a multi-bunch filling pattern, in a 'moderate' brilliance regime.

3.5. Hybrid filling pattern for improved slicing efficiency

The short pulse radiation performance reported in Table 2 is calculated for a uniformly filled train of bunches, *i.e.* same bunch charge for all bunches. However, equation (29) suggests that, to increase the total slicing efficiency, dedicated high-charge bunches should be used (Holldack *et al.*, 2014; Schick *et al.*, 2016). Multi-bunch coupled instabilities are enhanced by higher charge density, and typically are minimized by hybrid filling pattern, *i.e.* by temporal separation of ≥10 ns between bunches devoted to slicing and to all the others in a train. In the case of multiple bunches designed for slicing, such temporal separation must match the temporal gating of the detector, which is adopted to minimize the radiation background from sliced electrons on successive turns (see Section 1). Moreover, owing to the higher charge density, the sliced bunches will show a higher transverse emittance at equilibrium, primarily as a consequence of intra-beam scattering (Leemann, 2014). However, if the number of high charge bunches is small compared with the total charge, photon beamlines sensitive to diffraction-limited optics will not be affected considerably on a multi-turn multi-bunch basis.

As an example of hybrid filling pattern for Elettra 2.0, we consider four high charge-bunches. The filling pattern is reduced from the nominal 93% to 91% (392 RF buckets filled), while the total average current remains at the nominal 400 mA level. The time separation of the special bunches from the others is ±10 ns. Alternatively, a single high charge-bunch separated by ±40 ns from the rest of the train could be considered. Assuming a six-times higher bunch charge, the transverse emittances are estimated to double, while the energy spread and the bunch length at equilibrium are almost unchanged. As already discussed in Section 2, no microwave instability build up is foreseen at this current level. A 10 kHz laser repetition rate and a few mJ laser pulse energy over a ∼0.5 ps laser pulse duration produces an energy modulation amplitude of the order of 1%. The total slicing efficiency is at the level of 10^{-7}.

A more accurate evaluation of practical options for Elettra 2.0 and of expected laser-slicing performance is summarized in Table 3. For the sake of brevity, parameters not listed in Table 3 are assumed to be the same as in Table 2. On the basis of the observations in Section 2 on background mitigation, Option 2 results to be the most promising scenario. A 10 kHz repetition rate with slicing in sequence mode is similarly announced by Holldack *et al.* (2014). In detail, the following options are considered:

(i) All bunches have the nominal charge of 0.8 nC; ten bunches devoted to slicing are separated by ±6 ns from leading and trailing bunches; the filling pattern is reduced to 86% (344 mA). Laser parameters are: 0.8 ps FWHM pulse duration, 3 mJ pulse energy, 10 kHz repetition rate (30 W average power). This case is simulated in Section 3.

(ii) Four bunches, each with a charge of 4.8 nC, are selected for slicing; each bunch is separated by ±10 ns from leading and trailing bunches. The filling pattern is 92.5% (376 mA). Laser parameters are: 0.4 ps FWHM pulse duration, 4 mJ pulse energy and 10 kHz repetition rate (40 W average power).

(iii) Same as in (ii), but now with increased laser average power: 3 mJ pulse energy, 20 kHz repetition rate (60 W average power).

4. Final remarks

The analytical expressions in Appendix *A* have been benchmarked with theoretical and experimental studies reported in the literature (Zholents & Zolotorev, 1996; Ingold *et al.*, 2001,

2007; Nadji *et al.*, 2004; Yu *et al.*, 2011; Lau *et al.*, 2012; Schoenlein *et al.*, 2000*a*; Khan *et al.*, 2006; Holldack *et al.*, 2014; Labat *et al.*, 2018). For each case, the laser-induced energy modulation and the total slicing efficiency were calculated with equation (10) and equation (29). We typically found a discrepancy <5% and for few cases in the range 15–20% for the energy modulation amplitude, and by a factor <2 for the total slicing efficiency. This result translates into a discrepancy in the predicted average spectral flux within ∼50%. Part of the discrepancy, sometimes referring to reported measured quantities, can be attributed to the uncertainty about the full list of parameters actually adopted by the authors; often different laser options are investigated and not all the details of the machine set up are given at the same time. Moreover, it is unclear if different authors calculated the energy modulation amplitude as given here in equation (11) or with the exact expression in equation (10). Our conclusion is that our modelling captures the salient features of the laser–electron interaction and predicts the radiation flux and the related spectral properties from the radiator with an uncertainty smaller than a factor two.

Fig. 12 collects our calculations of the laser-slicing performance in theoretical and experimental studies, including the three options illustrated in Table 3 for Elettra 2.0. We conclude that energy modulation amplitude of ∼1% can be reached in Elettra 2.0 with a 400 fs FWHM-long laser pulse and 3 mJ pulse energy in the radiator. In spite of an about three times lower laser peak power with respect to state-of-the-art experiments (Holldack *et al.*, 2014; Labat *et al.*, 2018), the laser–electron interaction is predicted to be roughly twice as efficient, mainly by virtue of the about five times smaller laser spot size at the waist (higher electric field), as allowed by the diffraction-limited optics of the storage ring. Compared with state-of-the-art experiments carried out at BESSY II (Holldack *et al.*, 2014) and for a comparable energy modulation amplitude of 0.7%, laser slicing at Elettra 2.0 is expected to provide a ten times higher total slicing efficiency at the expense of a four times higher average laser power. In terms of photon flux per unit length of the X-ray pulse, the proposed scheme is at the same level as the demonstrated state-of-the-art. We stress that the hybrid filling pattern with high bunch charges, as well as slicing in sequence mode, is essential to the predicted performance.

One distinct feature of the proposed scheme is the transparency of the laser-slicing scheme to the diffraction-limited optics design of Elettra 2.0. Namely, modifications to neither the magnetic lattice nor to the spaces planned for installation of IDs is required. The relatively low dispersion function at the radiator translates into a pure 0.5 mm spatial separation of the long and short radiation pulses (contrary to the configurations implemented, *e.g.* in BESSY II and Soleil). This impasse can be solved by 1:1 imaging of the radiation source. At the second focus of the imaging system, a slit can be used to select either the very intense 100 ps-long radiation pulses or less intense 0.4 ps-long pulses. The additional spectral separation allowed by emission in a TGU enhances the SNR at the detector by at least one additional order of magnitude in total flux density.

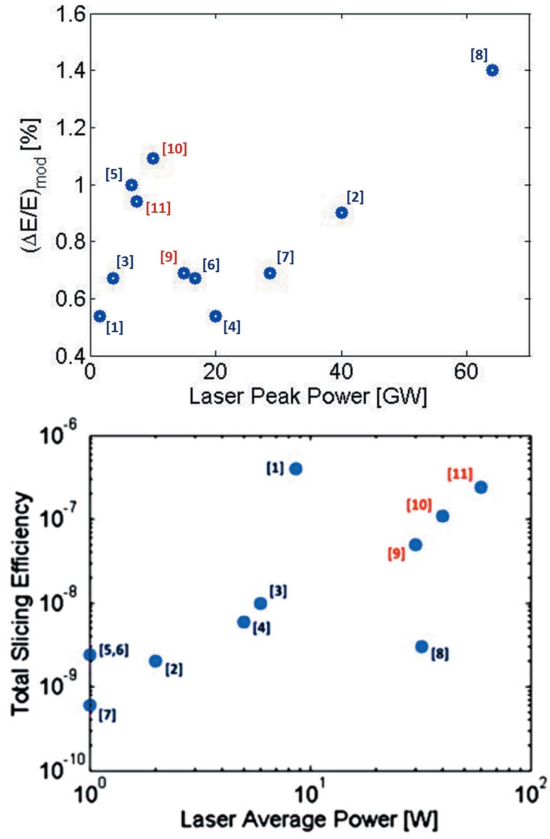

Figure 12
Top: on-axis relative energy modulation *versus* laser peak power (this is the laser pulse energy divided by the laser FWHM duration). Bottom: total slicing efficiency *versus* laser average power. [1] Zholents & Zolotorev (1996), [2] Khan *et al.* (2006), [3] Holldack *et al.* (2014), [4] Ingold *et al.* (2001), [5] Ingold *et al.* (2007), [6] Labat *et al.* (2018), [7] Yu *et al.* (2011), [8] Lau *et al.* (2012), [9] Elettra 2.0 – Option 1, [10] Elettra 2.0 – Option 2, [11] Elettra 2.0 – Option 3 (see Table 3).

APPENDIX *A*
Theoretical model of laser-slicing

A1. Energy modulation amplitude

We consider a linearly polarized wiggler (undulator parameter $K \gg 1$). The number of photons emitted per wiggler period by a single electron by incoherent (spontaneous) emission at the fundamental wavelength is (Jackson, 1999)

$$\frac{N_\gamma}{N_u} = \frac{2}{3}\pi\alpha\,\frac{K^2[JJ]^2}{1+K^2/2}, \tag{7}$$

where $\alpha \simeq 1/137$ is the fine-structure constant, $K = 0.934\,B_0[\mathrm{T}]\lambda_u[\mathrm{cm}]$ with B_0 the peak wiggler field, and $[JJ]$ is the electron-field coupling parameter (Jackson, 1999). The wavelength of emission at the nth harmonic ($n \geq 1$) is

$$\lambda_{R,n} = \frac{\lambda_u}{2\gamma^2 n}\left(1+\frac{K^2}{2}+\gamma^2\theta^2\right), \tag{8}$$

where θ is the observation angle with respect to the wiggler axis. The total energy radiated along N_u wiggler periods at the fundamental wavelength ($n = 1$) is

$$E_R = \frac{N_\gamma}{N_u} N_u \hbar\omega_R = \frac{2}{3}\pi\alpha \frac{K^2[JJ]^2}{1+K^2/2} N_u \hbar\omega_R. \quad (9)$$

We now consider a Gaussian and Fourier transform limited laser beam co-propagating with the electron beam and superimposed on it through the wiggler. The laser central wavelength is the same as the fundamental wavelength of the on-axis spontaneous emission, $\omega_R = \omega_L$. The electrons wiggling in the insertion device interact with the transverse electric field of the laser, and the energy exchange is proportional to the laser energy within the laser relative spectral bandwidth, $E_L(\Delta\omega_L/\omega_L)$. The energy modulation imposed by the laser on the electron beam is (Zholents & Zolotorev, 1996) $\Delta E^2_{mod} = 4E_R E_L(\Delta\omega_L/\omega_L)$ and, therefore, by virtue of equation (9),

$$\begin{aligned}\Delta E^2_{mod} &= \frac{8}{3}\pi\alpha \frac{K^2[JJ]^2}{1+K^2/2}\frac{\omega_R}{\Delta\omega_R}\hbar\omega_R E_L \frac{\Delta\omega_L}{\omega_L} \\ &\cong \frac{8}{3}\pi\alpha \frac{K^2/2}{1+K^2/2} E_L \hbar\omega_L \frac{\Delta\omega_L}{\Delta\omega_R}. \end{aligned} \quad (10)$$

Here we used the definition of wiggler relative spectral bandwidth $N_u \cong \omega_R/\Delta\omega_R$ and $[JJ]^2 \to 1/2$ for $K > 3$. Since the ratio of the laser and wiggler bandwidths is equivalent to the number of wiggler periods N_u over the number of laser cycles N_L, and since the energy modulation becomes rather insensitive to K for $K \gg 1$, we can approximate equation (10) by

$$\Delta E^2_{appr} \simeq 4\pi\alpha E_L \hbar\omega_L \frac{N_u}{N_L}. \quad (11)$$

A2. Energy spread

In the approximation of a sinusoidal variation of the laser electric field with time, the r.m.s. energy spread associated with the on-axis energy modulation amplitude is $\sigma_{E,mod} = \Delta E_{mod}/\sqrt{2}$. A more realistic picture of the laser–electron interaction takes into account both the laser and the electron beam transverse size, σ_E and σ_L, as well as their variation along the wiggler. To do this, we revisit the expression given by Huang *et al.* (2004), initially derived, for example, by Tran & Wurtele (1989), which expresses the r.m.s. laser-induced energy spread as a function of the laser peak power P_L; this quantity is intended to be the laser energy per pulse duration, within the relative spectral bandwidth of the laser,

$$\sigma_{E,mod} = (m_e c^2)\left(\frac{P_L}{P_0}\right)^{1/2} \frac{K[JJ]}{\gamma}\frac{L_u}{\sqrt{2}\sigma_L} \Im_x(L_u)\Im_y(L_u), \quad (12)$$

with

$$\Im_{x,y}(L_u) = \frac{1}{L_u}\int_{-L_u/2}^{L_u/2} dz \frac{\sigma_L}{\left[\sigma^2_{e,(x,y)}(z) + \sigma^2_L(z)\right]^{1/2}}. \quad (13)$$

In equation (13) we introduced the following quantities: $P_0 = (m_e c^2)^2/(\alpha\hbar) = 8.7$ GW, $L_u = N_u\lambda_u$ is the wiggler length, and the laser beam's intensity envelope is assumed to be round, which is not necessarily the case for the electron beam. The waist of the laser and of the electron beam is assumed to be in the middle of the wiggler, so that $\bar\sigma_L = (\lambda\bar Z_R/\pi)^{1/2}$ is the laser transverse size at the waist calculated for the Rayleigh length that minimizes the laser spot at the wiggler edges, *i.e.* $\bar Z_R = L_u/2$. It is worth recalling that, neglecting any focusing by the wiggler field of the electron beam envelope, the laser and the electron beam envelope evolves from the waist as follows,

$$\sigma^2_e = \varepsilon\left(\beta_0 + \frac{z^2}{\beta_0}\right), \qquad \sigma^2_L = \sigma^2_{L,w}\left(1 + \frac{z^2}{Z^2_R}\right), \quad (14)$$

where ε is the geometric or natural electron beam transverse emittance, β_0 is the betatron function at the waist, and $\sigma_{L,w}$ is the laser size at the waist. We point out that $\Im_{x,y}(L_u) \to 1$ for a zero-emittance electron beam, and in the approximation $\sigma_L(z) = \bar\sigma_L$ all along the wiggler; $\Im_{x,y}(L_u) \to 1/2$ when the electron beam size matches the aforementioned 'optimum' laser size. For a vanishing electron beam size and an optimum laser size, equation (12) shows that, as expected, the smaller the laser size in the wiggler, the larger the energy modulation will be by virtue of the increased electric field amplitude of the laser pulse.

Below we demonstrate that equation (12) is identical to the r.m.s. energy spread derived from equation (11) for negligible electron beam sizes and minimum average laser spot size $\{\bar\sigma_L = [\lambda L_u/(2\pi)]^{1/2}\}$ along the wiggler ($K > 3$),

$$\begin{aligned}\sigma^2_{E,mod} &= (m_e c^2)^2 \frac{P_L}{(m_e c^2)^2}\alpha\hbar \frac{K^2[JJ]^2}{\gamma^2}\frac{L^2_u}{2\lambda L_u} 2\pi\Im_x\Im_y \\ &\cong 2\pi\alpha\hbar E_L\omega_L \frac{\Delta\omega_L}{\omega_L}\frac{K^2/2}{\lambda_u(1+K^2/2)} N_u\lambda_u \\ &= 2\pi\alpha\hbar\omega_L E_L \frac{K^2/2}{(1+K^2/2)}\frac{\Delta\omega_L}{\Delta\omega_R} \\ &\simeq 2\pi\alpha E_L\hbar\omega_L \frac{N_u}{N_L} = \frac{\Delta E^2_{appr}}{2}. \end{aligned} \quad (15)$$

Equation (15) shows that the energy modulation amplitude given by Zholents & Zolotorev (1996) is in fact the maximum amplitude expected in ideal conditions. In this article we adopted the more realistic expression in equation (10) for the on-axis energy modulation amplitude induced by the laser–electron interaction, and in equation (12) for the corresponding energy spread.

A3. Pulse length

The photon pulse duration σ_{ph} is estimated by Zholents & Zolotorev (1996) as the quadratic sum of the laser pulse duration σ_L, the slippage of radiation over the electrons along the wiggler (typically negligible for laser pulses of femtosecond duration or longer), and the elongation of the portion of laser-sliced electrons due to the electron beam transport from the wiggler to the radiation source σ_l,

$$\sigma_{ph} \cong \left(\sigma^2_L + \sigma^2_l\right)^{1/2}. \quad (16)$$

σ_L depends on the transport matrix terms of the magnetic lattice from the wiggler to the radiation source that are coupled to the beam size, angular divergence (horizontal only in the absence of vertical dispersion) and relative energy

spread evaluated at the wiggler location. In the linear approximation,

$$\sigma_l^2 = R_{51}^2\sigma_x^2 + R_{52}^2\sigma_{x'}^2 + R_{56}^2\sigma_{\delta,\mathrm{mod}}^2. \quad (17)$$

It can be shown (Di Mitri & Cornacchia, 2014) that, to first order in the particle coordinates, the first two terms on the right-hand side of equation (17) are approximately equal to $\varepsilon_x\langle H_x\rangle_s$, where the H_x function is averaged over the length of the beamline from the wiggler to the radiation source,

$$H_{xs} = \frac{1}{\Delta s}\int_0^s \mathrm{d}z\left(\gamma_x\eta_x^2 + 2\alpha_x\eta_x\eta_x' + \beta_x\eta_x'^2\right), \quad (18)$$

and η_x, η_x' are the energy dispersion function and its longitudinal derivative; γ_x, α_x, β_x are the so-called Courant–Snyder or Twiss parameters. The last term on the right-hand side of equation (17) can be written in terms of the storage ring momentum compaction and the length of the beamline from the wiggler to the radiation source,

$$\sigma_l^2 \cong \varepsilon_x\langle H_x\rangle_s + \alpha_c^2\Delta s^2\sigma_{\delta,\mathrm{mod}}^2. \quad (19)$$

The result is that a low-emittance storage ring favours the preservation of short radiation pulses through the ring by virtue of both small emittance and small average H_x function.

A4. Equilibrium, repetition rate and modulation efficiency

We next write the equation for the variation of the relative energy spread with time in the presence of radiation damping and laser slicing. In the following, $\sigma_{\delta,0}$ is intended to be the natural (equilibrium) relative energy spread in the absence of laser excitation. Radiation damping tends to reduce the energy spread exponentially with time, on the typical time scale of $\tau_D \simeq 10$ ms. Laser-slicing enlarges the energy spread over of the bunch portion $\Delta t_{sl}/\Delta t_b$ interacting with the laser, at the laser repetition rate $1/\tau_{sl} = f_L/N_b$, with N_b the number of bunches in the stored bunch train interacting with the laser, and f_L the laser frequency,

$$\frac{\mathrm{d}\sigma_\delta^2}{\mathrm{d}t} = \frac{\left(\sigma_{\delta,0}^2 - \sigma_\delta^2\right)}{\tau_D} + \frac{\sigma_{\delta,\mathrm{mod}}^2}{\tau_{sl}}\frac{\Delta t_{sl}}{\Delta t_b}. \quad (20)$$

By imposing equation (20) equal to zero, we find the relative energy spread at equilibrium,

$$\sigma_{\delta,\mathrm{eq}}^2 = \sigma_{\delta,0}^2 + \left(\frac{f_L\Delta t_{sl}}{N_b\Delta t_b}\tau_D\right)\sigma_{\delta,\mathrm{mod}}^2 \equiv \sigma_{\delta,0}^2 + \frac{\tau_D}{\tau_g}\sigma_{\delta,\mathrm{eq}}^2, \quad (21)$$

where, following Zholents & Zolotorev (1996), we defined the ratio of the laser-induced energy modulation over the new equilibrium energy spread, and therefore the energy spread growth rate,

$$\frac{1}{\tau_g} = \frac{p^2 f_L\Delta t_{sl}}{2N_b\Delta t_b}. \quad (22)$$

From equation (21) we also have

$$\frac{1}{\tau_g} = \frac{1}{\tau_D}\left(1 - \frac{\sigma_{\delta,0}^2}{\sigma_{\delta,\mathrm{eq}}^2}\right). \quad (23)$$

Equation (23) can be used to specify the minimum value of τ_g for any maximum tolerable ratio $\sigma_{\delta,\mathrm{eq}}/\sigma_{\delta,0}$ (*e.g.* smaller than 1.5). Such a tolerance translates through equation (22) into a specification for the maximum laser pulse repetition rate.

The physical meaning of the p-parameter is related to the number of electrons brought to the energy amplitude required for spatial/angular/spectral separation of the short pulse radiation from background radiation. As the energy modulation is sinusoidal with the electron-laser relative phase, the larger energy modulation amplitude – *i.e.* better separation from the non-sliced electrons – corresponds to fewer electrons moved to the off-energy level. In addition, radiation from only half of those electrons (either at the positive or negative off-energy level) will be collected. For these reasons, a larger energy separation leads to better signal-to-noise ratio of the emitted radiation at the expense of lower flux. Zholents & Zolotorev (1996) defined the electron capturing efficiency η_1 in a way that, for a betatron size of the electron beam negligible with respect to the chromatic beam size at the radiator, *i.e.* $\sigma_{x,\mathrm{tot}} \simeq \sigma_{x,\eta}$, it satisfies

$$1 - \cos(\pi\eta_1) = \frac{1}{2p}. \quad (24)$$

Thus, η_1 is maximum and equal to 1 for the amplitude of energy modulation equal to a quarter of the energy spread at equilibrium, in the presence of slicing. Experimental evidence (Schoenlein *et al.*, 2000*a*; Ingold *et al.*, 2007; Holldack *et al.*, 2014; Labat *et al.*, 2018) suggest a value $p \simeq 4$–10 for an acceptable SNR, and therefore the efficiency turns out to be bounded to the range $\eta_1 \simeq 0.1$–0.2.

A5. Radiation from dipole magnet and undulator

The spectral energy distribution of radiation emitted by a single electron in a dipole magnet is (Jackson, 1999)

$$\frac{\mathrm{d}E_{\mathrm{ph}}}{\mathrm{d}\omega} = \frac{\mathrm{d}\left(N_{\mathrm{ph}}\hbar\omega\right)}{\mathrm{d}\omega} = \frac{\sqrt{3}}{4\pi\varepsilon_0}\frac{e}{c^2}\gamma\frac{\omega}{\omega_c}\int_{\omega/\omega_c}^{\infty}\mathrm{d}x\ K_{5/3}(x), \quad (25)$$

where $\omega_c = (3/2)\gamma^3(c/R)$ is the critical frequency of dipole magnet synchrotron radiation in terms of the beam energy Lorentz factor γ, the light speed in vacuum c, and the dipole bending radius R. $K_{5/3}$ is the second-order modified Bessel function. Thus, the number of photons emitted per unit spectral bandwidth is

$$\frac{\mathrm{d}N_{\mathrm{ph}}}{\mathrm{d}\omega/\omega} = \frac{\mathrm{d}E_{\mathrm{ph}}}{\mathrm{d}\omega}\frac{\omega}{\hbar\omega} = \sqrt{3}\alpha\gamma\frac{\omega}{\omega_c}\int_{\omega/\omega_c}^{\infty}\mathrm{d}x\ K_{5/3}(x) \quad (26)$$

or

$$\frac{\mathrm{d}N_{\mathrm{ph}}}{\mathrm{d}\omega/\omega_c} = \sqrt{3}\alpha\gamma\int_{\omega/\omega_c}^{\infty}\mathrm{d}x\ K_{5/3}(x). \quad (27)$$

Once divided by the beam revolution period in the storage ring and taking into account both the total number of N_e electrons in the bunch and the total slicing efficiency ξ_{sl} (see

below), equation (27) turns into the expression given by Zholents & Zolotorev (1996) for the total number of photons emitted per unit time (intensity), per unit azimuthal angle (defined over the entire range 0–2π) and unit relative spectral bandwidth,

$$\left(\frac{\mathrm{d}N_{\mathrm{ph}}}{\mathrm{d}t\,\mathrm{d}\theta\,\mathrm{d}\omega/\omega}\right)_{\mathrm{sl,dip}} = \frac{\sqrt{3}}{2\pi}\alpha\gamma\frac{\omega}{\omega_{\mathrm{c}}}\int_{\omega/\omega_{\mathrm{c}}}^{\infty}\mathrm{d}x\;K_{5/3}(x)\,\frac{N_{\mathrm{e}}}{T_{\mathrm{riv}}}\xi_{\mathrm{sl}} \qquad (28)$$

$$= N_{\mathrm{e}}\frac{\sqrt{3}}{2\pi}\alpha\gamma\left[\frac{\omega}{\omega_{\mathrm{c}}}\int_{\omega/\omega_{\mathrm{c}}}^{\infty}\mathrm{d}x\;K_{5/3}(x)\right]\eta_1\frac{\Delta t_{\mathrm{sl}}}{\Delta t_{\mathrm{b}}}\frac{I_{\mathrm{sl}}}{I_{\mathrm{b}}}f_{\mathrm{L}}.$$

The slicing efficiency is defined as (Zholents & Zolotorev, 1996; Holldack *et al.*, 2014)

$$\xi_{\mathrm{sl}} = \eta_1\frac{\Delta t_{\mathrm{sl}}}{\Delta t_{\mathrm{b}}}\frac{f_{\mathrm{L}}}{f_{\mathrm{riv}}}\frac{I_{\mathrm{sl}}}{I_{\mathrm{b}}}, \qquad (29)$$

where f_{riv} is the single bunch revolution frequency and $I_{\mathrm{sl}}/I_{\mathrm{b}}$ is the ratio of average currents of the total stored beam and of a *single* sliced bunch. In other words, $f_{\mathrm{riv}}(I_{\mathrm{b}}/I_{\mathrm{sl}})$ is the effective repetition rate of short photon pulses. Note that equation (22) holds for arbitrarily large f_{L}, which is assumed to be consistent with the maximum tolerable equilibrium energy spread [see equation (23)]. If, instead, f_{L} is limited by the maximum laser average power, the equilibrium energy spread will be determined by equations (22) and (23) (Zholents & Zolotorev, 1996).

ξ_{sl} applies identically to any parameter associated with the radiation emitted by a bunch in a storage ring (spectral brilliance, flux, angular intensity, *etc.*). The existing literature gives its value in the range 10^{-8}–10^{-9} for optimized practical situations. So, for example, the number of photons emitted per second at the nth harmonic by a laser-sliced electron bunch in a short undulator and unit relative bandwidth, integrated over the central angular cone of amplitude

$$2\pi\sigma_{r'}^2 = \frac{\pi}{2\gamma^2}\frac{1+K^2/2}{nN_{\mathrm{u}}} = \pi\frac{\lambda_n}{L_{\mathrm{u}}},$$

is

$$\left(\frac{\mathrm{d}N_{\mathrm{ph}}}{\mathrm{d}t\,\mathrm{d}\omega/\omega}\right)_{\mathrm{sl,und}} = \frac{\pi}{2}\frac{\alpha N_{\mathrm{u}}}{n}\frac{I}{e}\left(1+\frac{K^2}{2}\right)n^2\frac{K^2}{(1+K^2/2)^2}[JJ]_n^2\,\xi_{\mathrm{sl}}$$

$$= \pi\alpha N_{\mathrm{u}}\frac{I}{e}\frac{K^2/2}{(1+K^2/2)}n\,[JJ]_n^2\,\xi_{\mathrm{sl}}, \qquad (30)$$

where I stands for the electron beam (average or peak) current, and $[JJ]_n$ is the undulator's field-electron coupling factor calculated for the nth harmonic. The factor $n^2[JJ]_n^2K^2/(1+K^2/2)$ in the first equality of equation (30) has a value around 0.4 for n = 3–9 (Kim, 1995).

Acknowledgements

Two of the authors (SDM and WAB) acknowledge Professor F. Parmigiani for stimulating briefings on the generation of short pulses, and E. Karantzoulis for providing the lattice of Elettra 2.0.

References

Bane, K., Cai, Y. & Stupakov, G. (2010). *Phys. Rev. ST Accel. Beams*, **13**, 104402.
Beaud, P., Johnson, S. L., Streun, A., Abela, R., Abramsohn, D., Grolimund, D., Krasniqi, F., Schmidt, T., Schlott, V. & Ingold, G. (2007). *Phys. Rev. Lett.* **99**, 174801.
Borland, M. (2000). *elegant: A Flexible SDDS-Compliant Code for Accelerator Simulation.* Presented at the *6th International Computational Accelerator Physics Conference (ICAP2000)*, 11–14 September 2000, Darmstadt, Germany. Report No. LS-287.
Borland, M. (2014). *Synchrotron Radiat. News*, **27**(6), 2–3.
Byrd, J. M., Hao, Z., Martin, M. C., Robin, D. S., Sannibale, F., Schoenlein, R. W., Zholents, A. A. & Zolotorev, M. S. (2006). *Phys. Rev. Lett.* **96**, 164801.
Cerrina, F. & Sanchez del Rio, M. (2009). In *Handbook of Optics*, Vol. V, 3rd ed., ch. 35, edited by M. Bass. New York: McGraw-Hill.
Di Mitri, S. & Cornacchia, M. (2014). *Nucl. Instrum. Methods Phys. Res. A*, **735**, 60–65.
Holldack, K., Bahrdt, J., Balzer, A., Bovensiepen, U., Brzhezinskaya, M., Erko, A., Eschenlohr, A., Follath, R., Firsov, A., Frentrup, W., Le Guyader, L., Kachel, T., Kuske, P., Mitzner, R., Müller, R., Pontius, N., Quast, T., Radu, I., Schmidt, J.-S., Schüßler-Langeheine, C., Sperling, M., Stamm, C., Trabant, C. & Föhlisch, A. (2014). *J. Synchrotron Rad.* **21**, 1090–1104.
Holldack, K., Khan, S., Mitzner, R. & Quast, T. (2006). *Phys. Rev. Lett.* **96**, 054801.
Huang, Z., Borland, M., Emma, P., Wu, J., Limborg, C., Stupakov, G. & Welch, J. (2004). *Phys. Rev. ST Accel. Beams*, **7**, 074401.
Ingold, G., Beaud, P., Johnson, S. L., Gromlind, D., Schlott, V., Schmidt, Th. & Streun, A. (2007). *Synchrotron Rad. News*, **20**(5), 39.
Ingold, G., Streun, A., Singh, B., Abela, R., Beaud, P., Knopp, G., Rivkin, L., Schlott, V., Schmidt, Th., Sigg, H., van der Veen, J. F., Wrulich, A. & Khan, S. (2001). *Proceedings of the 2001 Particle Accelerator Conference (PAC2001)*, 18–22 June 2001, Chicago, IL, USA, pp. 2656–2658. WPPH085.
Jackson, J. D. (1999). *Classical Electrodynamics*, 3rd ed. New York: John Wiley and Sons.
Karantzoulis, E. (2018). *Nucl. Instrum. Methods Phys. Res. A*, **880**, 158–165.
Karantzoulis, E. & Barletta, W. (2019). *Nucl. Instrum. Methods Phys. Res. A*, **927**, 70–80.
Khan, S., Holldack, K., Kachel, T., Mitzner, R. & Quast, T. (2006). *Phys. Rev. Lett.* **97**, 074801.
Kim, K.-J. (1995). *Opt. Eng.* **342**, doi:10.1117/12.194193.
Labat, M., Brubach, J.-B., Ciavardini, A., Couprie, M.-E., Elkaim, E., Fertey, P., Ferte, T., Hollander, P., Hubert, N., Jal, E., Laulhé, C., Luning, J., Marcouillé, O., Moreno, T., Morin, P., Polack, F., Prigent, P., Ravy, S., Ricaud, J.-P., Roy, P., Silly, M., Sirotti, F., Taleb, A., Tordeux, M.-A. & Nadji, A. (2018). *J. Synchrotron Rad.* **25**, 385–398.
Lau, W. K., Chou, M. C., Hwang, C. S., Lee, A. P., Liu, Y. C., Luo, G. H. & Huang, N. Y. (2012). *Proceedings of the Third International Particle Accelerator Conference (IPAC2012)*, 20–25 May, New Orleans, LA, USA, pp. 1671–1673. TUPPP027.
Leemann, S. (2014). *Phys. Rev. ST Accel. Beams*, **17**, 050705.
Martin, I. P. S. (2011). PhD Thesis, Wolfson College, University of Oxford, UK (https://ora.ox.ac.uk/objects/uuid:9ac0bcc2-bedb-46d0-b95c-22f4741f45a0).
Nadji, A., Chubar, O., Idir, M., Level, M.-P., Loulerge, A., Moreno, T., Nadolski, L. & Polack, F. (2004). *Proceedings of the 9th Particle Accelerator Conference (EPAC2004)*, 5–7 July 2004, Lucerne, Switzerland, pp. 2332–2334. THPKF029.
Prigent, P., Hollander, P., Labat, M., Couprie, M. E., Marlats, J. L., Laulhé, C., Luning, J., Moreno, T., Morin, P., Nadji, A., Polack, F.,

Ravy, S., Silly, M. & Sirotti, F. (2013). *J. Phys. Conf. Ser.* **425**, 072022.
Raimondi, L. & Spiga, D. (2015). *A A*, **573**, A22.
Raimondi, L., Svetina, C., Mahne, N., Cocco, D., Abrami, A., De Marco, M., Fava, C., Gerusina, S., Gobessi, R., Capotondi, F., Pedersoli, E., Kiskinova, M., De Ninno, G., Zeitoun, P., Dovillaire, G., Lambert, G., Boutu, W., Merdji, H., Gonzalez, A. I., Gauthier, D. & Zangrando, M. (2013). *Nucl. Instrum. Methods Phys. Res. A*, **710**, 131–138.
Schick, D., Le Guyader, L., Pontius, N., Radu, I., Kachel, T., Mitzner, R., Zeschke, T., Schüßler-Langeheine, C., Föhlisch, A. & Holldack, K. (2016). *J. Synchrotron Rad.* **23**, 700–711.
Schoenlein, R. W., Chattopadhyay, S., Chong, H. H., Glover, T. E., Heimann, P. A., Leemans, W. P., Shank, C. V., Zholents, A. A. & Zolotorev, M. S. (2000*b*). *Appl. Phys. B*, **71**, 1–10.
Schoenlein, R. W., Chattopadhyay, S., Chong, H. H., Glover, T. E., Heimann, P. A., Shank, C. V., Zholents, A. A. & Zolotorev, M. S. (2000a). *Science*, **287**, 2237–2240.
Schoenlein, R. W., Elsaesser, T., Holldack, K., Huang, Z., Kapteyn, H., Murnane, M. & Woerner, M. (2019). *Philos. Trans. R. Soc. A*, **377**, 20180384.
Streun, A. (2003). *SLS-FEMTO: beam halo formation and maximum repetition rate for laser slicing.* Report SLS-TME-TA-2003-0222. Paul Scherrer Institut, CH-5232 Villigen PSI, Switzerland.
Tanaka, T. & Kitamura, H. (2001). *J. Synchrotron Rad.* **8**, 1221–1228.
Tran, T. M. & Wurtele, J. S. (1989). *Comput. Phys. Commun.* **54**, 263–272.
Venturini, M. & Warnock, R. (2002). *Phys. Rev. Lett.* **89**, 224802.
Yu, L. H., Blednykh, A., Guo, W., Krinsky, S., Li, Y., Shaftan, T., Tchoubar, O., Wang, G. M., Willeke, F. & Yang, L. (2011). *Proceedings of the 2011 Particle Accelerator Conference (IPAC2011)*, 28 March–3 April 2011, New York, USA, pp. 2381–2383. THP136.
Zholents, A. A. & Zolotorev, M. S. (1996). *Phys. Rev. Lett.* **76**, 912–915.